Bioorg. Med. Chem. 111 (2024) 117849

Contents lists available at ScienceDirect

Bioorganic & Medicinal Chemistry

journal homepage: www.elsevier.com/locate/bmc

New substituted benzoxazine derivatives as potent inducers of membrane permeability and cell death

Ana Conejo-García [a,b], Yaiza Jiménez-Martínez [c,d], Rubén Cámara [a], Francisco Franco-Montalbán [a], Jesús Peña-Martín [c,d], Houria Boulaiz [b,c,d,*], M. Dora Carrión [a,b,**]

[a] Department of Medicinal and Organic Chemistry and Excellence Research Unit of Chemistry Applied to Biomedicine and the Environment, Faculty of Pharmacy, Campus Cartuja s/n, University of Granada, 18071 Granada, Spain
[b] Biosanitary Institute of Granada (ibs.GRANADA), SAS-University of Granada, Avenida de Madrid, 15, 18012 Granada, Spain
[c] Department of Anatomy and Human Embryology, Faculty of Medicine, Avenida de la Investigación 11, University of Granada, 18016 Granada, Spain
[d] Biopathology and Regenerative Medicine Institute (IBIMER), Avenida del Conocimiento s/n, 18016 Granada, Spain

ARTICLE INFO

Keywords:
Benzoxazines
Antitumor
Cell death
Membrane permeability and cell cycle arrest

ABSTRACT

The search for new agents targeting different forms of cell death is an important research focus for developing new and potent antitumor therapies. As a contribution to this endeavor, we have designed and synthesized a series of new substituted 3,4-dihydro-2*H*-1,4-benzoxazine derivatives. These compounds have been evaluated for their efficacy against MCF-7 breast cancer and HCT-116 colon cancer cell lines. Overall, substituting this heterocycle led to improved antiproliferative activity compared to the unsubstituted derivative **1**. The most active compounds, **2b** and **4b**, showed IC_{50} values of 2.27 and 3.26 μM against MCF-7 cells and 4.44 and 7.63 μM against HCT-116 cells, respectively. To investigate the mechanism of action of the target compounds, the inhibition profile of 8 kinases involved in cell signaling was studied highlighting residual activity on HER2 and JNK1 kinases. **2b** and **4b** showed a consistent binding mode to both receptor kinases, establishing significant interactions with known and catalytically important domains and residues. Compounds **2b** and **4b** exhibit potent cytotoxic activity by disrupting cell membrane permeability, likely triggering both inflammatory and non-inflammatory cell death mechanisms. This dual capability increases their versatility in the treatment of different stages or types of tumors, providing greater flexibility in clinical applications.

1. Introduction

Today, cancer is one of the most significant public health challenges globally, causing nearly 10 million deaths in 2022. The World Health Organization has predicted that the new cases of cancer will reach 35 million by 2050.[1]

The four cancers with the highest incidence are breast, lung, colorectal, and prostate cancer.[2] Breast cancer is the most common cancer in women worldwide and colorectal cancer is the third most prevalent form of primary malignancy.[3] The significant morbidity and mortality associated with these two cancers is a major public health problem, making research and development of new molecules with therapeutic utility in these cancers critical.[4]

Signaling pathways associated with cancer include those involved in cell proliferation, differentiation, and survival. These pathways represent promising targets for the development of novel antitumor drugs. In this way kinases play an important role in the development and progression of several types of cancer.[5] The overexpression of the human epidermal growth factor receptor-2 (HER2) is related to several tumors, including breast and colorectal cancer.[6–8] It is overexpressed in 15–30 % of invasive breast cancers, which has both prognostic and predictive implications. The c-Jun NH_2-terminal kinases (JNKs) are protein kinases involved in a variety of cellular activities, including cell apoptosis, an important mechanism of tumor suppression.[9] Thus, kinome profiling has emerged as an interesting tool involved in cancer pathology.[10]

To develop effective treatments for cancer and other diseases

* Corresponding author at: Department of Anatomy and Human Embryology, Faculty of Medicine, Avenida de la Investigación 11, University of Granada, 18016 Granada, Spain.
** Corresponding author at: Department of Medicinal and Organic Chemistry and Excellence Research Unit of Chemistry Applied to Biomedicine and the Environment, Faculty of Pharmacy, Campus Cartuja s/n, University of Granada, 18071 Granada, Spain.
E-mail addresses: hboulaiz@ugr.es (H. Boulaiz), dcarrion@ugr.es (M.D. Carrión).

https://doi.org/10.1016/j.bmc.2024.117849
Received 20 June 2024; Received in revised form 17 July 2024; Accepted 22 July 2024
Available online 24 July 2024

characterized by dysregulated cell death, understanding the diverse mechanism that lead to cell viability loss and eventual demise is crucial. Membrane permeabilization stands as a pivotal event in the spectrum of cell death processes, encompassing apoptosis, necrosis, pyroptosis, and others.[11–13] Antitumor therapeutic strategies targeting cell membrane permeabilization can be effective and promising in certain contexts. Inducing membrane permeabilization in tumor cells can activate regulated cell death pathways such as apoptosis or pyroptosis. In contrast to apoptosis, where membrane permeabilization is a controlled process that restricts the release of intracellular contents and mitigates inflammatory responses, pyroptosis involves membrane permeabilization as a pro-inflammatory event that enhances immune responses and may contribute to the development of inflammatory diseases.[14] Membrane permeability also plays a critical role in non-regulated cell death, such as necrosis. During this process, the plasma membrane becomes permeable in a non-selective manner, leading to leakage of cellular components into the surrounding environment. This loss of membrane integrity is a hallmark of necrosis and reflects disruption of cellular homeostasis.[12] Developing antitumor treatments capable of inducing cell death through multiple pathways offers significant advantages in terms of overcoming resistance, enhancing selectivity, promoting therapeutic synergy, and adapting to the clinical and biological diversity present in patients with cancer and other diseases.[15]

Several benzoxazine derivatives with antitumor activity have been published previously.[16–19] In addition, 1,4-benzoxazine derivatives show activity against, diabetes, neurodegenerative, inflammatory, autoimmune and cardiovascular diseases.[20,21]

We previously published a series of 1,4-benzoxazine derivatives with antitumor properties (Fig. 1).[22] The most interesting compound (**1**) showed IC_{50} values of 13.00 μM against MCF-7 breast cancer cells and 7.06 μM against HCT-116 colon cancer cells. The search for new agents that target different forms of cell death is an important research focus for the development of new and potent antitumor agents.

Here, we present a new series of 3,4-dihydro-2*H*-1,4-benzoxazines linked to substituted purine rings (derivatives **2a–d**, **3a–d**, and **4a–d**, Fig. 1) with the aim to develop potent antitumor agents. We have retained the 6-membered benzoxazine ring of derivative **1** by introducing different substituents in positions 6 or 7. For the first time, we have slightly deactivated (Cl and Br, compounds **2** and **3**) and activated (CH_3, compounds **4**) the benzofused ring (Fig. 1). To obtain structure–activity relationships, we have introduced different substituents in the purine moiety (6-Cl series **a**, 2,6-diCl series **b**, 6-Br series **c**, and 6-CF_3 series **d**).

2. Results and discussion

2.1. Chemistry

The general synthetic route to achieve the target derivatives **2a–d**, **3a–d** and **4a–d** is summarized in Scheme 1.

The synthesis starts with the reaction between the corresponding

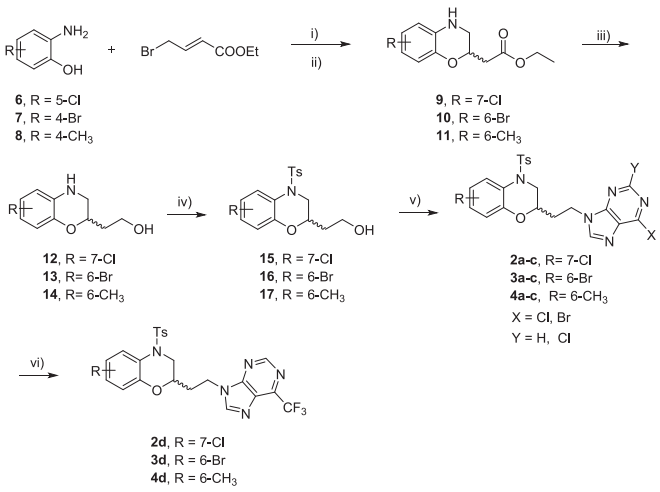

Scheme 1. Synthesis of benzoxazines **2a–d**, **3a–d**, and **4a–d**. *Reagents and conditions*: (i) $NaHCO_3$, EtOH, 3 h, rt; (ii) K_2CO_3 30 min; (iii) $LiAlH_4$, Et_2O, 1 h, 0 °C to rt; (iv) TsCl, pyr, 12 h, 0 °C to rt; (v) 6-halopurine or 2,6-dihalopurine, DIAD, Ph_3P, THF, 36 h, −20 °C to rt; (vi) derivative **2c**, **3c** or **4c**, MFSDA, CuI, HMAP, DMF, microwaves 150 °C 15 min.

commercial aminophenol **6–8** and ethyl 4-bromobut-2-enoate in a basic medium. First, nucleophilic substitution takes place with release of the bromide ion, followed by cyclization to give the derivatives **9–11** in good yields (85–88 %). The ester group is then reduced to the primary alcohol using $LiAlH_4$ as reducing agent[23] to give compounds **12–14** (87–89 % yield). Then, the tosylation of the benzoxazine ring is carried out by nucleophilic substitution using tosyl chloride and pyridine to give derivatives **15–17** in high yields of 87–89 %.[24] Subsequently, the Mitsunobu reaction[25] using the corresponding 6-halopurine or 2,6-dihalopurine, triphenylphosphine and diisopropylazidecarboxylate (DIAD) in anhydrous tetrahydrofuran (THF) gives the target compounds substituted with chlorine and bromine on the purine ring **2a–c**, **3a–c** and **4a–c** (82–87 % yield). Finally, starting from the bromine derivatives **2c**, **3c** or **4c** the bromine is exchanged with the trifluoromethyl group using fluorosulfonyldifluoromethyl acetate (MFSDA), CuI, hexamethylphosphoramide (HMPA) and dimethyformamide (DMF) as solvent,[26] this reaction was carried out in microwave at 150 °C for 15 min with high yields between 78–80 %.

2.2. In vitro antiproliferative activity

We first evaluated the effects of the target compounds on cell proliferation in the human breast cancer cell line MCF-7 and the human colon carcinoma cell line HCT-116. These two cancers are currently among the top 20 most deadly ones, underlining the urgent need to develop novel treatments. The antiproliferative activity of **2a–d**, **3a–d** and, **4a–d** was evaluated using the sulforhodamine B colorimetric assay after 72 h of treatment (Table 1). Derivative **1** is included as a reference

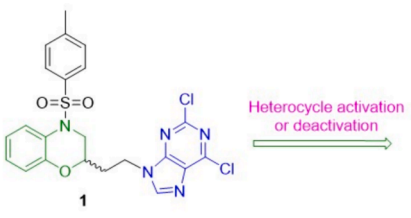

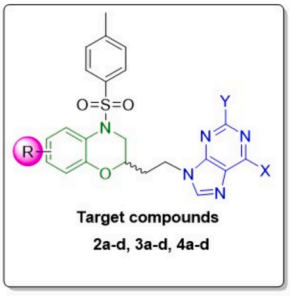

Comp.	R	X	Y
2a	7-Cl	Cl	H
2b	7-Cl	Cl	Cl
2c	7-Cl	Br	H
2d	7-Cl	CF_3	H
3a	6-Br	Cl	H
3b	6-Br	Cl	Cl
3c	6-Br	Br	H
3d	6-Br	CF_3	H
4a	6-CH_3	Cl	H
4b	6-CH_3	Cl	Cl
4c	6-CH_3	Br	H
4d	6-CH_3	CF_3	H

Fig. 1. Chemical structures of our previously reported benzoxazine and benzoxazepine derivatives (**1**, **2**), and target compounds (**2a–d**, **3a–d**, **and 4a–d**).

Table 1
Antiproliferative activities of compounds **3a–d**, **4a–d**, **5a–d** and **1** against MCF-7 and HCT-116 cancer cells.

Comp	R	X	Y	Cancer cell lines	
				IC_{50} MCF-7 (μM)	IC_{50} HCT-116 (μM)
2a	7-Cl	Cl	H	11.23 ± 0.70	14.76 ± 2.62
2b	7-Cl	Cl	Cl	3.26 ± 0.08	7.63 ± 0.33
2c	7-Cl	Br	H	6.77 ± 0.29	12.77 ± 1.60
2d	7-Cl	CF_3	H	22.98 ± 4.07	13.58 ± 2.58
3a	6-Br	Cl	H	14.47 ± 3.53	15.65 ± 0.58
3b	6-Br	Cl	Cl	5.52 ± 0.90	7.85 ± 0.25
3c	6-Br	Br	H	7.31 ± 0.10	16.40 ± 1.89
3d	6-Br	CF_3	H	20.61 ± 1.77	23.57 ± 3.11
4a	6-CH_3	Cl	H	12.86 ± 1.21	23.80 ± 3.64
4b	6-CH_3	Cl	Cl	2.27 ± 0.61	4.44 ± 0.33
4c	6-CH_3	Br	H	4.01 ± 0.11	9.40 ± 0.97
4d	6-CH_3	CF_3	H	31.13 ± 1.00	4.63 ± 1.00
1[22]	H	Cl	Cl	13.00 ± 0.11	7.06 ± 0.80

All experiments were conducted in duplicate and gave similar results. Data are mean ± SD of three independent determinations. MCF-7: human breast cancer cell line and HCT-116: human colon cancer cell line.

compound.

All compounds generally showed similar activities in both cell lines. The most active compound, **4b**, had an IC_{50} of 2.27 μM and 4.44 μM against MCF-7 and HCT-116 cells, respectively (Table 1); it has a methyl substituent at position 6 of the benzofused ring and the 2,6-dichloropurine moiety.

Regarding the substitution of the 1,4-benzoxazine the presence of the methyl group is important for the biological activity, while the introduction of the chloro or bromo slightly decreased their antiproliferative activity (**4b** > **2b** > **3b**, IC_{50} MCF-7 = 2.27 > 3.26 > 5.52 μM, respectively). These compounds showed the same pattern of activity against HCT116 cells, although with slightly higher values (**4b** > **2b** > **3b**, IC_{50} HCT116 = 4.44 > 7.63 > 7.85 μM, respectively).

Thus, all compounds bearing the 2,6-dichloropurine moiety (**2b**, **3b**, and **4b**) showed the best antiproliferative activity in both tumor cell lines (≤7.85 μM). Replacement of 2,6-dichloropurine by bromo- chloro- or trifluoromethylpurine decreased the antiproliferative effect in all cases. Interestingly, the IC_{50} values in MCF-7 follow the same pattern in the three series of synthesized compounds (**2b** > **2c** > **2a** > **2d**; **3b** > **3c** > **3a** > **3d** and **4b** > **4c** > **4a** > **4d**), while in HCT-116 we observed minor differences.

In general, the substitution of this heterocycle resulted in better antiproliferative activity values compared to the unsubstituted compound **1**.

2.3. Kinase inhibition assays

To investigate the mechanism of action of these compounds, the five derivatives (**2b**, **2c**, **3b**, **4b** and **4c**) that showed the best antiproliferative activity values were tested on an inhibition profile of 8 kinases involved in cellular signaling that regulate cell growth, proliferation, differentiation, and survival. These kinases, including AKT2, AMPK alpha1, EGFR, HER2, ERK2, JNK1, and P38 alpha, along with the LKB1/MO25/STRADa complex, are frequently dysregulated in cancer, making them pivotal targets for therapeutic development. Table 2 shows the results obtained for the residual kinase activity at 2 concentrations, 5 μM and 50 μM.

In general, the compounds show a moderate level of residual kinase activity, with some interesting results at a concentration of 50 μM on the kinases HER2 and JNK1.

The most active compound **4b** against MCF-7 and HCT-116 showed 50 % and 56 % residual activity against HER2 and JNK 1 respectively, suggesting that some of its activity may be inhibiting these enzymes. This compound presents 6-methyl and 2,6-dichloropurine substituents. Compound **4c** with 6-bromopurine moiety instead of 2,6-dichloropurine of **4b** showed similar residual activities values, being slightly higher for HER2. Compound **2b** with chlorine in position 7 and 2,6-dichloropurine in position 2 of the benzoxazine showed moderate residual activities against HER2 and JNK1, being slightly higher than **4b** at 50 μM, the replacement of 2,6-dichloropurine by 6-bromopurine **3c** resulted in slightly lower values for the residual activity of both kinases. The substitution of the benzoxazine ring by a bromo in position 6 (**3b**) also leads to moderate inhibition values of the tested kinases, standing out the residual activity at 50 μM on JNK1.

HER2 is an essential protein for cell division and normal cell growth, and its aberrant overexpression has been linked to cancer processes associated with poor prognosis and decreased overall survival in patients.[27] JNK1 in MCF-7[28] and HCT-116[29] can be induced by cellular stress that promotes apoptosis. Therefore, the modulation of its activity

Table 2
Selective profiles of **2b**, **2c**, **3b**, **4b** and **4c** against 8 protein kinases.

Kinase	Conc	Comp.				
		2b	**2c**	**3b**	**4b**	**4c**
AKT2	5 μM	103	94	95	88	89
	50μM	139	99	87	104	106
AMPK alpha1	5 μM	87	90	86	93	90
	50μM	89	73	70	75	86
EGFR	5 μM	74	108	94	96	97
	50μM	57	64	59	62	67
HER2	5 μM	76	84	78	90	99
	50μM	67	65	63	50	55
ERK2	5 μM	93	90	86	88	81
	50μM	94	68	66	73	74
JNK1	5 μM	78	89	88	96	84
	50μM	67	47	44	56	52
LKB1/MO25/ STRADa	5 μM	84	94	98	88	95
	50μM	100	129	95	89	131
P38 alpha	5 μM	72	91	97	112	93
	50μM	77	112	59	82	70

Residual activity > 25 % and < 55 %.
Residual activity > 55 % and ≤ 75 %.
Residual activity > 75 %.

may be an interesting therapeutic strategy to induce apoptosis in cancer cells.

2.4. Computational studies

The most interesting compounds **2b** and **4b** were subjected to docking analysis to gain some insight into their molecular binding mode to both HER2 and JNK1 kinases. The critical residues for the catalytic activity of kinase receptors are often found in the ATP-binding site at the interface of the C- and *N*-lobes formed by the C-helix, and the A-loop, a dynamic feature that is a common site for phosphorylation that regulates kinase activity. Some of the key residues typically involved are the DFG motif (Asp-Phe-Gly), at the *N*-terminal end of the A-loop, which is critical for coordinating metal ions and aligning the ATP for phosphorylation, and the P-loop which is involved in binding the phosphate groups of ATP.[30]

As these compounds are purine analogues, the ATP-binding site was explored as the purported inhibition site. Following the criteria used in our previous publication,[8] human HER2 (hHER2, pdb ID: 3RCD)[31] was used to study the molecular interactions in both enantiomers of the above compounds. This protein is crystallized with a pyrrolo-pyrimidine inhibitor, **TAK-285**, at the ATP binding site of the receptor. As a control, **TAK-285** was first redocked on the hHER2 crystal structure, and the resulting binding pose is almost identical to that in the crystal structure, in particular the disposition of the pyrrolo-pyrimidine cycle, the h-bond to Met801, and the two phenyl rings at one end of the molecule (Fig. 2). The only difference is the position of the tertiary hydroxyl tail that in the redocked position h-bonds Asp863 -of the DFG motif- and Lys753, whereas in the crystallized pose this moiety is oriented towards the P-loop, which h-bonds the backbone chain of Gly727.

Next, the molecular interactions of compounds **2b** and **4b** were evaluated. Regarding the docking poses of **4b**, both enantiomers show the purine ring in the hinge region where cognate ligand (**TAK-285**) places its pyrrolopyrimidine ring, forming a h-bond with the backbone chain of Met801. The main difference is the orientation of their benzoxazine rings that are displayed in opposite directions. In the *S*-enantiomer, this ring is located toward a pocket situated at the entrance of the catalytic site, made by residues Ser1002, Thr1003, Asp808, His809, and Glu812. The oxygen atom of the oxazine ring h-bond Cys805 at the entrance of the pocket. The *R*-enantiomer, however, orients its benzoxazine ring in an opposite direction, toward Asp863 of the DFG motif. As for the phenylsulfonamide moiety on both enantiomers, it is displayed toward the entrance of the catalytic pocket and near residues Leu726 and Gly727 in the P-loop (Fig. 3A). Likewise, both enantiomers of ligand **2b**, display their purine moiety in the same fashion as (*R*)- and (*S*)-**4b**. In addition, their benzoxazine moiety sit toward the same pocket, situated at the entrance of the catalytic site. This moiety is π-stacking Phe1004, at the entrance of the pocket, and its chlorine atom is well inserted into the pocket cavity. However, the phenylsulfonamide moiety is oriented with a slightly different orientation towards the solvent-exposed region (Fig. 3B).

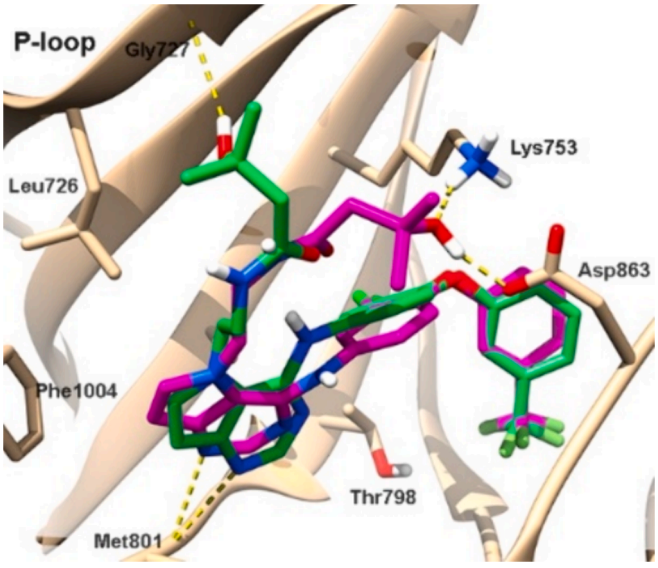

Fig. 2. Superposition of the predicted binding pose (purple) and crystallized binding pose (green) of **TAK-285** on hHER2 (pdb ID 3RCD, tan). Hydrogen bonds are shown as dashed yellow lines. (For interpretation of the references to colour in this figure legend, the reader is referred to the web version of this article.)

Ligands, **2b** and **4b** were also docked on the human JNK1 kinase isoform (hJNK1, pdb ID 4AWI). Both compounds show a slightly different binding pattern when compared to hHER2. (*R*)- and (*S*)-**2b** display its purine moiety toward the C-helix, forming h-bonds with the conserved Lys55 residue on β3. Their benzoxazines are set on the hinge region showing stacking interactions with Leu168 at the hinge region and Val40 on the *N*-lobe, and the *p*-phenylsulfonamide moiety is displayed on the solvent-exposed region with (*R*)-**4b** h-bonding the backbone chain of Met111 at the hinge region through one of the oxygen atoms of its sulfonamide group (Fig. 4A). (*R*)- and (*S*)-**2b** also display their purine heterocycles toward the C-helix, forming h-bonds with the conserved Lys55 on β3, in like manner as ligands (*R*)- and (*S*)-**4b**. However, their benzoxazines are not set on the hinge region but to the solvent-exposed area with their chlorine atom pointing out. A second conformational difference between (*R*)- and (*S*)-**2b**, and (*R*)- and (*S*)-**4b** lay on the orientation of the *p*-phenylsulfonamide. In (*R*)- and (*S*)-**2b** this moiety is displayed toward the hinge region and in a hydrophobic region set by Ala53, Leu110, Met111, Val158, and Leu168 (Fig. 4B).

In summary, ligands **2b** and **4b** show a consistent binding mode to hHER2 and hJNK1 catalytic domain, establishing significant interactions with well stablished and catalytically important domains and residues of both kinase receptors. These interactions might help explaining their moderate kinase activity and suggest future potential chemical modifications that could enhance their binding affinity.

2.5. Scanning electron microscopy

We selected the highly effective compounds **2b** and **4b** for further investigation against colon cancer HCT-116 cells and breast cancer MCF-7 cells to explore their effects on cellular morphology. High concentrations of drugs are often used for short periods of time in mechanistic studies to achieve maximal pharmacological effects within a limited time frame. This strategy facilitates the delineation of precise pathways and mechanisms by which the drug modulates cellular processes. For that, for the remaining experiments, we opted for a concentrated regimen of 50 μM compounds, thereby reducing treatment durations to 12 h.

Through scanning electron microscopy (SEM), the hallmarks of various types of cell death have been discerned by tracking patterns and events. SEM revealed significant morphological alterations in HCT-116 control cells exhibited abundant microvilli extensions on their surface and displayed strong adherence to the culture flask surface (Fig. 5A and B). However, when treated with **2b** and **4b**, HCT-116 colon cancer cells exhibited cells with different morphology and varied responses to the treatment (Fig. 5C and H). While some cells retained their microvilli, others did not. Instead, they showed the presence of multiple cellular remnants, significant formation of vesicular bodies, membrane blebbing and a noticeable flattening of the cellular structure. Additionally, the presence of pores was observed in some cells, especially notable in cells treated with compound **2b**. Similar results were observed in MCF-7 breast cancer cells treated with **2b** and **4b**. While the control group exhibited rounded cells densely populating the culture, with surfaces covered with microvilli (Fig. 5I and J), the treated cells displayed cells with different morphology and size (Fig. 5K and P). Some were

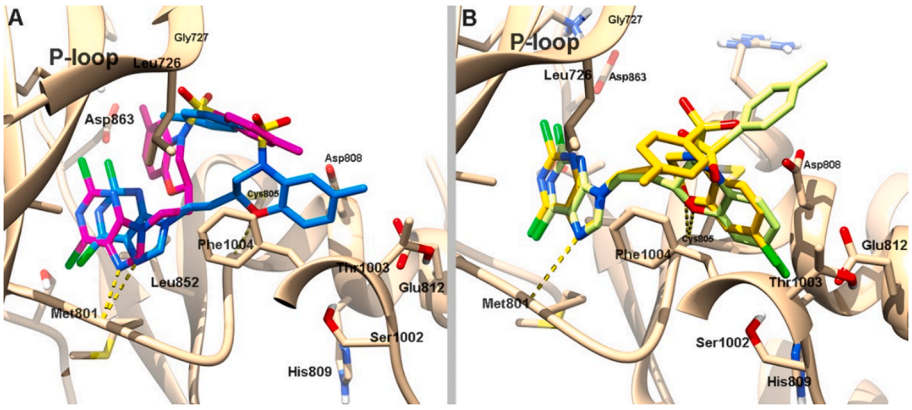

Fig. 3. (**A**) Predicted binding poses of (*R*)-**4b** (purple) and (*S*)-**4b** (blue), on hHER2 (pdb ID 3RCD, tan); (**B**) predicted binding poses of (*R*)-**2b** (lime) and (*S*)-**2b** (yellow), on hHER2 (pdb ID 3RCD, tan). (For interpretation of the references to colour in this figure legend, the reader is referred to the web version of this article.)

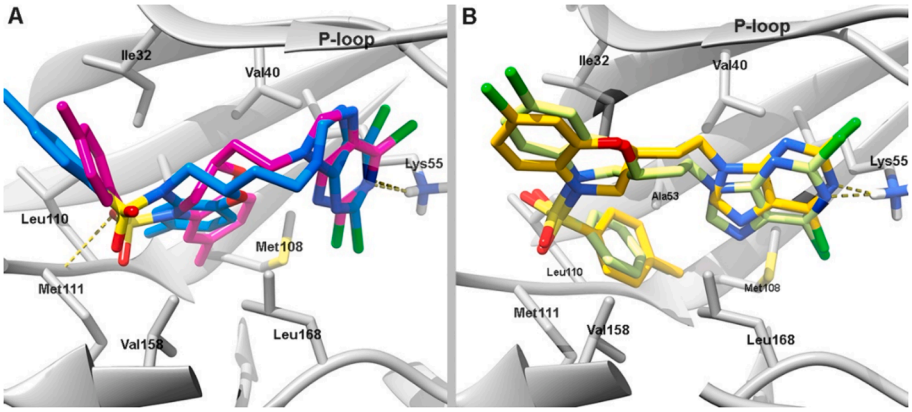

Fig. 4. (**A**) Predicted binding poses of (*R*)-**4b** (purple) and (*S*)-**4b** (blue), on hJNK1 (pdb ID 4AWI, grey); (**B**) Predicted binding poses of (*R*)-**2b** (lime) and (*S*)-**2b** (yellow), on hJNK1 (pdb ID 4AWI, grey). Hydrogen bonds are represented as dashed yellow lines. (For interpretation of the references to colour in this figure legend, the reader is referred to the web version of this article.)

completely destroyed, leading to the scattering of their cellular contents throughout the culture matrix, while others showed notable membrane disruption and a reduction in filopodia and microvilli. Additionally, SEM images revealed the presence of membrane blebbing, round vesicular bodies and large pores in the cell membranes of some cells.

The variety of morphological changes observed suggests that the **2b** and **4b** compounds induce cell death through multiple pathways. Certainly, the observed features in some cells, including their reduced size, the presence of wrinkled morphology with membrane blebbing, and the emergence of bodies, strongly suggest apoptosis. However, the identification of pores on the surface of some swollen cells indicates the involvement of another programmed cell death pathway, namely pyroptosis.[32] Furthermore, apoptotic bodies are generated during apoptosis, whereas pyroptotic bodies are produced during pyroptosis.[33] It is intriguing that the diameter of pyroptotic bodies is comparable to that of apoptotic bodies, both ranging from 1 to 5 μm.[34] This duality in cellular responses underscores the complexity of the mechanisms triggered by the studied compounds and leads us to conduct molecular studies to try to decipher its mechanism of action and the potential implication of both forms of cell death.[35]

2.6. Confirmation of membrane permeability induced by compounds 2b and 4b using annexin V binding assay

The morphological changes observed following treatment with **2b** and **4b** led us to suspect that the cytotoxicity of these compounds is mediated by damage on cell membrane, suggesting the existence of a membrane-induced mechanism of cell death. The annexin V assay utilizes annexin V, a protein with a high affinity for phosphatidylserine (PS), and propidium iodide (PI), a DNA-binding dye that only enters cells with compromised membranes and commonly used to identify apoptotic cells. This combination allows for the differentiation between viable cells (annexin V negative, PI negative), early apoptotic cells (annexin V positive and propidium iodide (PI) negative), and late apoptotic or necrotic cells (both annexin V and PI positive).

HCT-116 control cells showed 86.06 ± 0.66 % viability, 7.6 ± 0.57 % early apoptosis, 2.8 ± 0.38 % late-stage apoptosis, and 3.5 ± 0.66 % necrosis ($P<0.05$). In HCT-116 cells treated with **2b** and **4b**, we observed that there was an increase in late-stage apoptosis population 49.5 ± 2.7 % and 26.5 ± 1.7 % respectively (Fig. 6A–C and G). Furthermore, in both compounds, a notable increase in the necrotic cell population has been observed reaching 28.4 ± 2 % and 36.3 ± 1.7 % for **2b** and **4b** respectively.

In MCF-7 control culture (Figs. 6D–F and 3H), 98.8 ± 0.12 % of the cells were viable, 0.33 ± 0.12 % were in early apoptosis, 0.26 ± 0.09 % were in the late stages of apoptosis, and 0.56 ± 0.04 % were in necrosis. Interestingly, after 24 h of treatment with the novel compounds, the MCF-7 cell line exhibited a significant increase in the subpopulation undergoing late apoptosis compared to the control cells, with percentages ranging from 87.3 ± 1 % to 77.8 ± 1.8 %. Additionally, there was a slight increase in the percentage of early apoptosis with 7.9 ± 0.3 % and 9.3 ± 0.5 % in **2b** and **4b** respectively and necrotic cells compared to the control, with 0.83 ± 0.2 % in **2b** and 2.1 ± 1.2 % in **4b** ($P < 0.001$).

Our results indicate that both compounds significantly affect cell

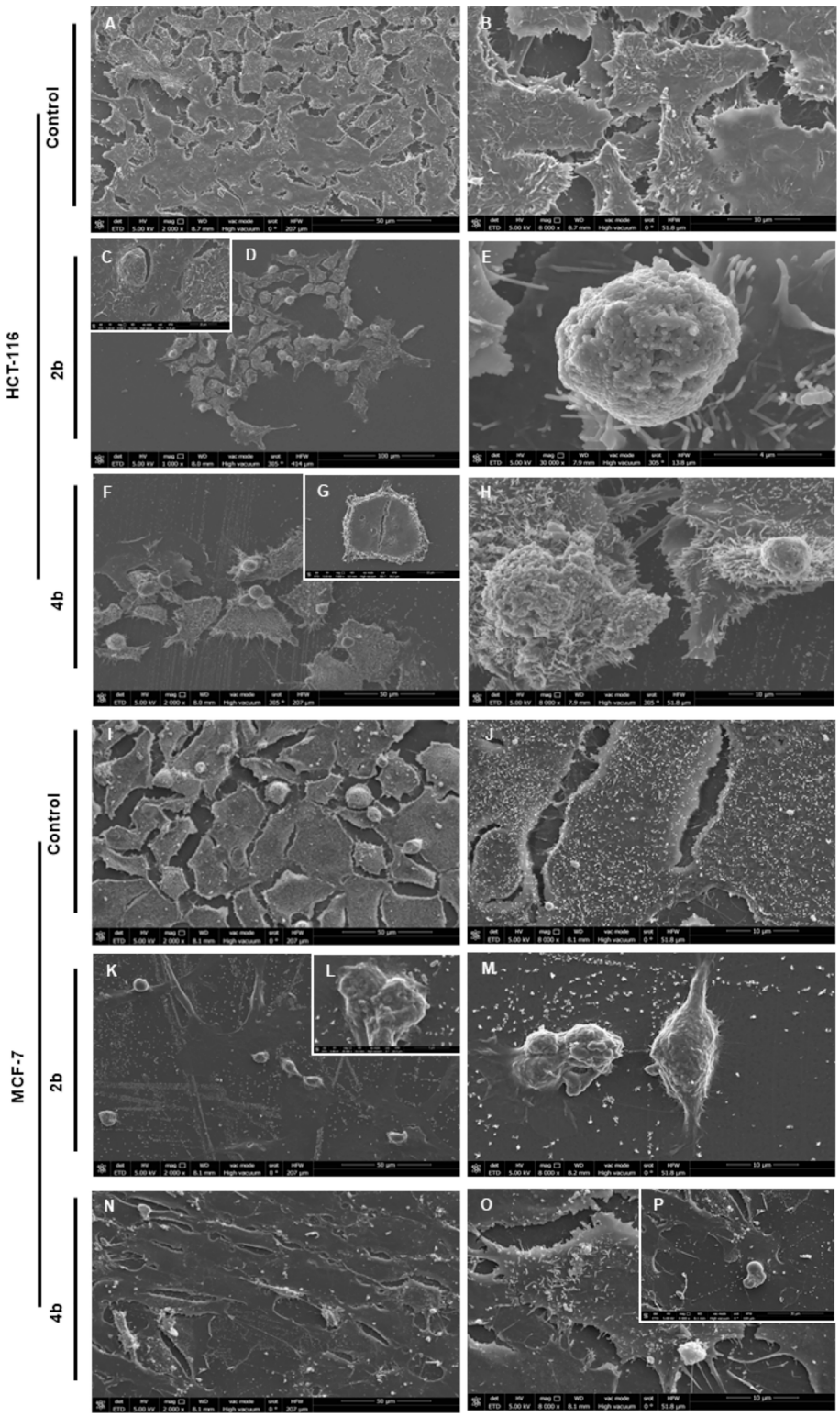

Fig. 5. Scanning electron microscopy of: HCT-116 cells control (A, B), treated by **2b** (C–E) and **4b** (F–H) and MCF-7 cells control (I, J) treated by **2b** (K–M) and **4b** (N–O). Treatment with compounds **2b** and **4b** (C, E, F, H) in the HCT-116 cell line resulted in cells exhibiting varied sizes and disrupted membrane structures. Observations included the presence of pores (H and E), large, flattened cells and a significant formation of vesicular bodies (C and G). Similarly, the MCF-7 cell line showed comparable effects following treatment with compounds **2b** and **4b**, including cells of different sizes with altered membranes, leading to the complete destruction of some cells (5K-P) and the dispersion of their contents throughout the culture matrix. Additionally, some cells displayed vesicular bodies and a reduction in filopodia and microvilli (M).

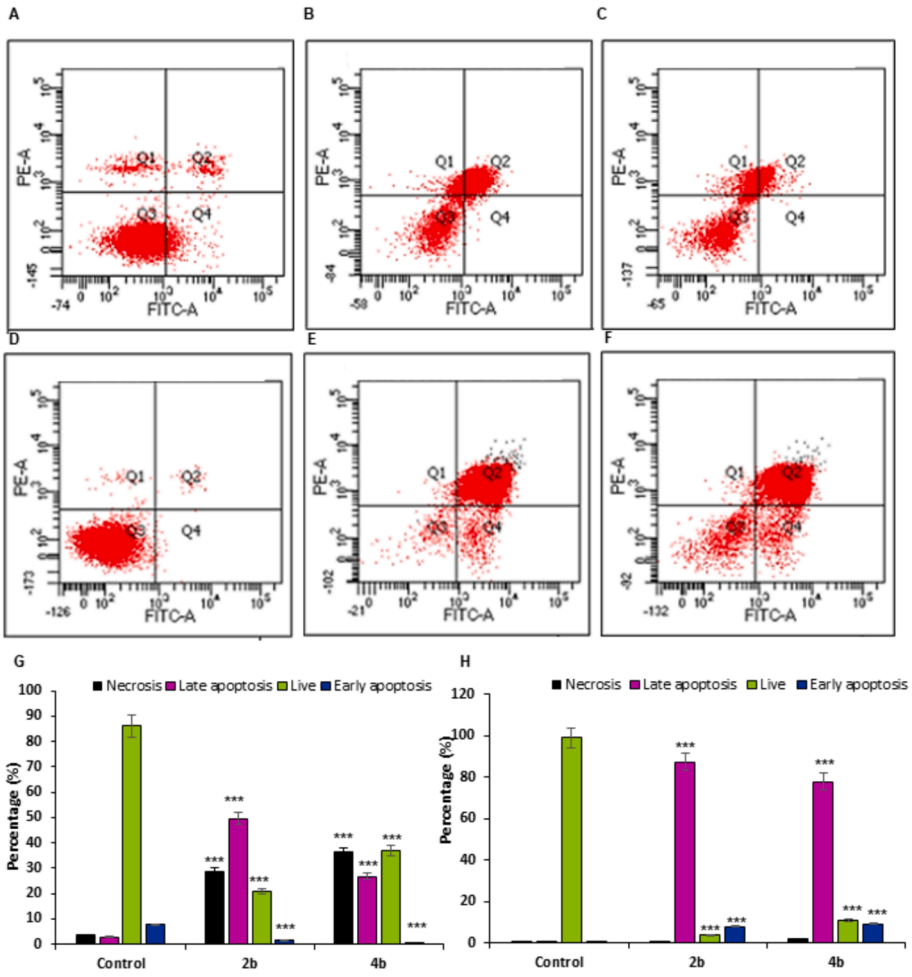

Fig. 6. Apoptosis images of HCT-116 colon cancer (A, B and C) and MCF-7 (D, E and F) breast cancer cells treated by **2b** and **4b**. Percentage of HCT-116 (G) and MCF-7 (H) in apoptosis. Data are expressed as the mean ± SD of the mean of three independent experiments (** $p < 0.01$ vs. control and *** $p < 0.001$ vs. control).

survival, resulting in an increased proportion of cells with compromised membranes positive both for annexin V and PI indicating late stage of apoptosis.[36] Interestingly, the presence of pores in the cell membrane of pyroptotic cells observed by SEM facilitates the binding of annexin V to PS. As a result, annexin V stains pyroptotic cells in the same way as apoptotic cells, making it unable to distinguish between the two programed cell death.[37,38]

On the other hand, our results showed that both compounds significantly increase the necrotic population, enhancing their effectiveness as anticancer agents especially in the HCT-116 cell line potentially. Similar effects were observed following treatment with other antitumor agents in several cancer cells.[39–41] This necrosis is classified as post-apoptotic secondary necrosis, representing the natural outcome of the complete apoptotic program as described by Silva.[42] In fact, when apoptotic cells are abundant *in vitro* or when the organism's phagocytic capacity is overwhelmed, apoptotic cells progress to a secondary necrosis stage, gradually losing their structural integrity. They undergo ballooning, plasma membrane permeabilization, and ultimately release cytoplasmic contents.[43] They regulation of secondary necrosis is an important and non-accidental process that has gained significant attention in recent years.[44] In fact, recent research has shown that the molecules released from the cytoplasm or exposed on the cell surface vary between primary necrosis, secondary necrosis, and regulated necrosis such as necroptosis.[43] Inducing secondary necrosis deliberately can enhance the immune response against tumors.[11] Compounds that modulate the apoptotic pathways to promote secondary necrosis can help in creating a pro-inflammatory environment that attracts immune cells to the tumor site, enhancing anti-tumor immunity.[45,46]

2.7. *2b and 4b treatment leads to s phase accumulation in HCT-116 cells*

In oncology, the uncontrolled proliferation of cells stands as one of the six recognized hallmarks of cancer. Within this context, the sustained inhibition of the cell cycle has emerged as a beneficial strategy in cancer therapeutics. To study whether the antiproliferative effect of **2b** and **4b** compounds involves changes in cell-cycle distribution, HCT-116 and MCF-7 cell lines were treated using the 50 μM for 12 h and then analyzed by flow cytometry. Cell cycle assays based on DNA content discriminate between the G0/G1, S, and G2/M cell cycle phases.

HCT-116 cell culture contained 72.8 ± 0.16 % G0/G1 cells, 18.7 ± 0.5 % S-phase cells and 8.3 ± 0.74 % G2/M−phase cells. Notably, following treatment with **2b** and **4b**, HCT-116 cells exhibited a progressive reduction in G2/M−phase cells (6.67 ± 1 % and 5.3 ± 1 % for **2b** and **4b**, respectively), with a concomitant accumulation in the S-phase (49.2 ± 5 % and 51.25 ± 1.8 % for **2b** and **4b**, respectively). These results suggest that both **2b** and **4b** treatments may effectively inhibit cell cycle progression at the S-phase, leading to a decreased proliferation rate and potential cell cycle arrest in HCT-116 cells (Fig. 7A). S-phase cell cycle arrest been described as an outcome resulting from the treatment with various antitumor agents.[47–49] This S-phase accumulation indicates that the compounds interfere with DNA replication processes, potentially triggering a checkpoint response that halts further progression of the cell cycle. As a result, cells are unable to transition to subsequent phases, thereby reducing overall cell division

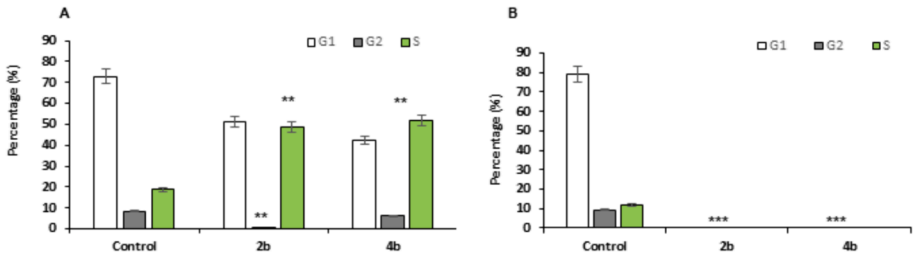

Fig. 7. Cell cycle of HCT-116 (A) and MCF-7(B) cancer cells treated by **2b** and **4b** vs Control. Data are expressed as the mean ± SD of the mean of three independent experiments (** $p < 0.01$ vs. control and *** $p < 0.001$ vs. control).

and proliferation. This mechanism of action highlights the potential of **2b** and **4b** as therapeutic agents in targeting rapidly dividing cancer cells by exploiting their dependency on continuous cell cycle progression. In contrast to HCT-116, the MCF-7 cell line was entirely obliterated despite receiving a high-dose treatment for only a brief duration. Consequently, assessing the cell cycle in cells treated with the two compounds proved unfeasible (Fig. 7B). This could be attributed to the heightened sensitivity of MCF-7 cells to the treatment, potentially associated with specific molecular pathways or genetic factors exclusive to this cell line.

3. Conclusions

We have designed and synthesized a series of substituted 3,4-dihydro-2*H*-1,4-benzoxazines. The antiproliferative effects of the target compounds against the cancer cell lines MCF-7 and HCT-116 were determined. Compounds bearing the 2,6-dichloropurine moiety in position 2 (**2b**, **3b**, and **4b**) showed the best antiproliferative activity in both tumor cell lines. However, the activity of the compounds is less affected by substitution at positions 6 or 7 by methyl, bromine or chlorine Compound **4b** exhibited the most promising activity against both tumor cell lines studied (IC_{50} MCF-7 = 2.27 μM and IC_{50} HCT-116 = 4.44 μM). Compared to the lead compound **1**, it demonstrated a 5.7-fold increase in activity against MCF-7 and a 1.5-fold increase in activity against HCT-116. While the IC_{50} values for HCT-116 (4.44 μM for compound **4b** and 7.06 μM for lead compound **1**) are within the same order of magnitude, compound **4b** still demonstrated a modest improvement in efficacy.

In general, the compounds exhibited moderate kinase inhibition values. **4b** showed residual activity of 50 and 56 % against HER2 and JNK1 respectively, a similar pattern of residual activity was shown for compound **2b**, albeit with slightly higher values. Computational studies show a consistent binding mode of **2b** and **4b** to the catalytic domains of hHER2 and hJNK1, forming significant interactions with key domains and residues critical for the catalytic activity of these kinase receptors.

This study is a proof of concept where our results suggest that compounds **2b** and **4b** exhibit a potent cytotoxic effect by disturbing membrane cell permeability triggering probably both inflammatory (secondary necrosis) and non-inflammatory (apoptosis) cell death mechanisms. This dual capability enhances their versatility in treating various stages or types of tumors, thereby providing greater flexibility in clinical applications. Furthermore, the ability to induce multiple forms of cell death may aid in overcoming drug resistance, a prevalent challenge in cancer therapy, by providing alternative pathways to eliminate resistant cells. However, further studies are necessary to identify specific biochemical pathways, molecular targets, gene expression profiles, and signaling cascades that underlie the observed outcomes at the molecular level. Exploring the molecular interactions and downstream effects of these compounds will provide deeper insights into their role in overcoming drug resistance and enhancing immune responses against tumors.

4. Experimental section

4.1. Chemistry

4.1.1. General remarks

All starting materials, reagents and solvents, were acquired from chemical companies. Analytical thin layer chromatography (TLC) was performed using Merck Kieselgel 60 F254 aluminium plates and visualised by UV light or iodine. All evaporations were carried out in vacuo in a Buchi rotary evaporator. Merck silicagel 60 with a particle size of 0.040–0.063 mm (230–400 mesh ASTM) was employed for flash chromatography. Small-scale microwave-assisted synthesis was carried out in an Initiator 2.0 single-mode microwave instrument producing controlled irradiation at 2.450 GHz (Biotage AB, Upsala, Sweden). ^{1}H NMR and ^{13}C NMR spectra were obtained using Bruker Avance NEO spectrometers with Smart Probe BBFO equipped, in the deuterated solvents. Chemical shifts are reported in ppm (δ ppm) and are referenced to the residual solvent peak. Spin multiplicities are given as s (singlet), d (doublet), dd (double doublet), t (triplet) and m (multiplet). *J* values are published in Hz. Electrospray ionisation (ESI-TOF) mass spectra were carried in a Bruker compact QTOF; source type: ESI, Ion Polarity positive or negative depending of the chemical structure of the compound, nebulizer 1.8 Bar, mass range 100–2000 *m/z*, capillary 4500 V positive mode or −4500 V negative mode, dry heater 220 °C and dry gas 9.0 l/min. Melting points were taken in open capillaries on a Stuart Scientific SMP3 electrothermal melting point apparatus and are uncorrected.

4.1.2. General method for the synthesis of ethyl 2-(6 or 7-substituted-3,4-dihydro-2H-benzo[b][1,4]oxazin-2-yl)acetate

To a solution of **6**–**8** (3.2 mmol) in EtOH (32 mL) under argon is added $NaHCO_3$ (540 mg, 6.4 mmol) and ethyl 4-bromobut-2-enoate (600 μL, 3.2 mmol). The reaction mixture is stirred at room temperature overnight. Then K_2CO_3 (442 mg, 3,2 mmol) is added and stirred for 2 h. Subsequently, the solvent is removed under vacuum and the residue is purified by flash chromatography (EtOAc/hexane 1:3).

*4.1.2.1. Ethyl 2-(7-chloro-3,4-dihydro-2H-benzo[b][1,4]oxazin-2-ylacetate (**9**). Brown oil; 85 % yield.* ^{1}H NMR (500 MHz, $CDCl_3$) δ 6.78 (d, 1H, *J*=2.3 Hz), 6.72 (dd, 1H, J_1 = 8.4, J_2 = 2.3 Hz, 1H), 6.50 (d, 1H, *J*=8.4 Hz), 4.58–4.53 (m, 1H), 4.22–4.16 (m, 1H), 3.46 (dd, 1H, J_1 = 11.7, J_2 = 2.5 Hz), 3.16 (dd, 1H, J_1 = 11.7, J_2 = 6.9 Hz), 2.75 (dd, 1H, J_1 = 15.8, J_2 = 6.8 Hz), 2.60 (dd, 1H, J_1 = 15.8, J_2 = 6.6 Hz), 1.28 (t, 3H *J*=7.1 Hz). ^{13}C NMR (126 MHz, $CDCl_3$) δ 170.22, 143.62, 131.56, 123.11, 121.20, 117.09, 115.89, 70.56, 60.87, 44.43, 37.79, 14.19. HRMS (ESI) *m/z* calcd for $C_{12}H_{15}NO_3Cl$ $[M+H]^{\pm}$ 256.0740; found 256.0755.

*4.1.2.2. Ethyl 2-(6-bromo-3,4-dihydro-2H-benzo[b][1,4]oxazin-2-ylacetate (**10**). Brown oil; 86 % yield.* ^{1}H NMR (300 MHz, $CDCl_3$) δ 6.76–6.75 (m, 2H), 6.64 (d, 1H, *J* = 9.1 Hz), 4.55 (dd, 1H, J_1 = 6.9, J_2 = 2.5 Hz), 4.21–4.16 (m, 2H), 3.49 (dd, 1H, J_1 = 11.7 Hz, J_2 = 2.5 Hz), 3.18 0.18 (dd, 1H, J_1 = 11.7, J_2 = 7.1 Hz, 1H), 2.75 (dd, 1H, J_1 = 15.9, J_2 = 6.7 Hz), 2.61 (dd, 1H, J_1 = 15.9, J_2 = 6.6 Hz), 1.31 (t, 3H, *J* = 7.0 Hz). ^{13}C

NMR (126 MHz, $CDCl_3$) δ 170.16, 142.38, 133.61, 121.182, 118.38, 117.85, 113.33, 70.26, 60.88, 44.26, 37.78, 14.19. HRMS (ESI) *m/z* calcd for $C_{12}H_{15}NO_3Br$ $[M+H]^+$ 300.0235; found 300.0256.

*4.1.2.3. Ethyl 2-(6-methyl-3,4-dihydro-2H-benzo[b][1,4]oxazin-2-ylacetate (**11**). Brown oil; 88 % yield.* ^{1}H NMR (500 MHz, $CDCl_3$) δ 6.68 (d, 1H, *J*=8.1 Hz), 6.48 (dd, 1H, $J_1 = 2.0$ Hz, $J_2 = 8.1$ Hz), 6.44 (d, 1H, $J = 2.0$ Hz), 4.58–4.53 (m, 1H), 4.19 (q, 2H, $J = 7.1$ Hz), 3.47 (dd, 1H, $J_1 = 11.6$, $J_2 = 2.5$ Hz), 3.18 (dd, 1H, $J_1 = 11.6$, $J_2 = 7.0$ Hz), 2.77 (dd, 1H, $J_1 = 15.7$, $J_2 = 6.6$ Hz), 2.61 (dd, 1H, $J_1 = 15.7$, $J_2 = 6.6$ Hz), 2.21 (s, 3H), 1.28 (t, 3H *J*=7.1 Hz). ^{13}C NMR (126 MHz, $CDCl_3$) δ 170.47, 141.13, 132.22, 130.81, 119.74, 116.69, 116.03, 70.35, 60.75, 44.78, 37.95, 20.71, 14.20. HRMS (ESI) *m/z* calcd for $C_{13}H_{18}NO_3$ $[M+H]^+$ 236.1287; found 236.1294.

4.1.3. General method for the synthesis of 2-(6 or 7-substituted-3,4-dihydro-2H-benzo[b][1,4]oxazin-2-yl)ethan-1-ol

Over a solution of 1 M $LiAlH_4$ (2.5 mL, 2.5 mmol) in anhydrous ethyl ether (19 mL) at 0 °C the corresponding derivative **9**–**11** (2.5 mmol) is added dropwise and stirred for 1 h. Then H_2O (3 mL) is added, and the resulting residue is extracted with Cl_2CH_2. After that, the organic phases are brought together, dried over anhydrous Na_2SO_4, filtered and concentrated under vacuum. The resulting residue is purified by flash chromatography (EtOAc/hexane 2:1).

*4.1.3.1. 2-(7-Chloro-3,4-dihydro-2H-benzo[b][1,4]oxazin-2-yl)ethan-1-ol (**12**). Orange oil; 87 % yield.* ^{1}H NMR (400 MHz, $CDCl_3$) δ 6.78 (d, 1H, *J*=2.3 Hz), 6.72 (dd, 1H, $J_1 = 8.4$, $J_2 = 2.3$ Hz), 6.50 (d, 1H, $J = 8.4$ Hz), 4.31–4.29 (m, 1H), 3.89–3.86 (m, 2H), 3.37 (dd, 1H, $J_1 = 11.7$, $J_2 = 2,4$ Hz), 3.16 (dd, 1H, $J_1 = 11.7$ Hz, $J_2 = 7.6$ Hz), 2.78 (s, 1H) 1.93–1.85 (m, 2H). ^{13}C NMR (101 MHz, $CDCl_3$) δ 143.86, 131.83, 122.95, 121.13, 116.92, 115.89, 72.37, 59.38, 45.22, 35.20. HRMS (ESI) *m/z* calcd for $C_{10}H_{13}NO_2Cl$ $[M+H]^+$ 214.0635; found 214.0630.

*4.1.3.2. 2-(6-Bromo-3,4-dihydro-2H-benzo[b][1,4]oxazin-2-yl)ethan-1-ol (**13**). Orange oil; 89 % yield.* ^{1}H NMR (500 MHz, $CDCl_3$) δ 6.77–6.75 (m, 2H) 6.64 (d, 1H, $J_1 = 9.1$ Hz), 4.32–4.28 (m, 1H), 3.92–3.84 (m, 2H), 3.41 (dd, 1H, $J_1 = 11.7$, $J_2 = 2.5$ Hz), 3.18 (dd, 1H, $J = 11.7$, 7.8 Hz), 3.05 (s, 1H), 1.97–1.84 (m, 2H). ^{13}C NMR (126 MHz, $CDCl_3$) δ 142.73, 133.62, 121.88, 118.24, 118.02, 113.30, 72.21, 59.44, 45.09, 35.17. HRMS (ESI) *m/z* calcd for $C_{10}H_{13}NO_2Br$ $[M+H]^+$ 258.0130; found 258.0131.

*4.1.3.3. 2-(6-Methyl-3,4-dihydro-2H-benzo[b][1,4]oxazin-2-yl)ethan-1-ol (**14**). Orange oil; 89 % yield.* ^{1}H NMR (400 MHz, $CDCl_3$) δ 6.68 (d, 1H, $J = 8.0$ Hz) 6.46 (dd, 1H, $J_1 = 8.0$, $J_2 = 2.0$ Hz), 6.45 (d, 1H, $J = 2.0$ Hz), 4.31–4.26 (m, 1H), 3.89–3.86 (m, 2H), 3.36 (dd, 1H, $J_1 = 11.7$, $J_2 = 2.4$ Hz) 3.19–3.14 (m, 1H), 2.97 (s, 1H), 2.21 (s, 3H), 1.98–1.80 (m, 2H).^{13}C NMR (126 MHz, $CDCl_3$) δ 141.34, 132.58, 130.86, 119.61, 116.53, 116.12, 72.55, 59.76, 45.59, 35.30, 20.73. HRMS (ESI) *m/z* calcd for $C_{11}H_{16}NO_2$ $[M+H]^+$ 194.1181; found 194.1173.

4.1.4. General method for the synthesis of 2-(6 or 7-substituted-4-tosyl-3,4-dihydro-2H-benzo[b][1,4]oxazin-2-yl)ethan-1-ol

To a solution of the corresponding benzoxazine **12**–**14** (1.14 mmol) and pyridine (137 μL, 1.7 mmol) in anhydrous CH_2Cl_2 (12 mL) at 0 °C, p-toluensulfonyl chloride (217 mg, 1.14 mmol) is added under argon atmosphere. The reaction mixture is stirred at room temperature overnight and then cold water is added and extracted with dichloromethane. Then, the organic phases are brought together and washed with 1 N HCl (3 mL) and brine. The organic phase is dried with anhydrous sodium sulphate, filtered and concentrated under vacuum. The crude obtained is purified by flash chromatography (EtOAc/hexane 1:3).

*4.1.4.1. 2-(7-Chloro-4-tosyl-3,4-dihydro-2H-benzo[b][1,4]oxazin-2-yl) ethan-1-ol (**15**). Orange oil; 87 % yield.* ^{1}H NMR (400 MHz, $CDCl_3$) δ 7.77 (d, 1H, *J*=8.9 Hz), 7.54–7.52 (m, 2H), 7.32–7.16 (m, 2H), 6.89 (dd, 1H, $J_1 = 8.9$ Hz, $J_2 = 2.4$ Hz), 6.53 (d, 1H, $J = 2.4$ Hz), 4.31 (dd, 1H, $J_1 = 14.5$ Hz, $J_2 = 2.3$ Hz), 3.76–3.72 (m, 2H), 3.56—3.50 (m, 1H), 3.15 (dd, 1H, $J_1 = 14.5$ Hz, $J_2 = 10.0$ Hz), 2.39 (s, 3H), 1.78–1.72 (m, 2H). ^{13}C NMR (101 MHz, $CDCl_3$) δ 147.23, 144.49, 135.23, 130.96, 129.97, 127.22, 125.12, 122.42, 121.07, 117.50, 70.14, 58.53, 48.43, 34.93, 21.56. HRMS (ESI) *m/z* calcd for $C_{17}H_{18}NO_4NaSCl$ $[M+Na]^+$ 390.0543; found 390.0513.

*4.1.4.2. 2-(6-Bromo-4-tosyl-3,4-dihydro-2H-benzo[b][1,4]oxazin-2-yl) ethan-1-ol (**16**). Orange oil; 88 % yield.* ^{1}H NMR (400 MHz, $CDCl_3$) δ 7.99 (d, 1H, $J = 2.4$ Hz), 7.56 (d, 2H, $J = 8.3$ Hz), 7.25 (d, 2H, $J = 8.3$ Hz), 7.12 (dd, 1H, $J_1 = 8.7$, $J_2 = 2.4$ Hz), 6.67 (d, 1H, $J = 8.7$ Hz), 4.30 (dd, 1H, $J_1 = 14.4$, $J_2 = 2.3$ Hz), 3.77–3.69 (m, 2H), 3.57–3.51 (m, 2H), 3.13 (dd, 1H, $J_1 = 14.4$ Hz, $J_2 = 9.8$ Hz), 2.38 (s, 3H), 1.82–1.69 (m, 2H). ^{13}C NMR (101 MHz, $CDCl_3$) δ 145.79, 144.67, 135.11, 130.06, 128.80, 127.29, 126.44, 124.91, 118.947, 112.71, 70.22, 58.59, 48.40, 34.96, 21.62. HRMS (ESI) *m/z* calcd for $C_{17}H_{18}NO_4SClBr$ $[M+Cl]^-$ 445.9828; found 445.9825.

*4.1.4.3. 2-(6-Methyl-4-tosyl-3,4-dihydro-2H-benzo[b][1,4]oxazin-2-yl) ethan-1-ol (**17**). Orange oil; 89 % yield.* ^{1}H NMR (400 MHz, $CDCl_3$) δ 7.64 (s, 1H), 7.55–7.52 (m, 2H), 7.26–7.22 (m, 2H), 6.84 (dd, 1H, $J_1 = 8.5$, $J_2 = 2.2$ Hz), 6.68 (dd, 1H, $J_1 = 8.5$ Hz, $J_2 = 1.6$ Hz), 4.30–4.25 (m, 1H), 3.74 (t, 2H, $J = 5.9$ Hz), 3.56–3.49 (m, 1H), 3.19–3.12 (m, 1H), 2.38 (s, 3H), 2.31 (s, 3H), 1.80–1.71 (m, 2H). ^{13}C NMR (101 MHz, $CDCl_3$) δ 144.45, 144.21, 135.66, 130.40, 129.86, 127.27, 126.82, 124.39, 123.28, 117.04, 70.07, 58.98, 48.80, 35.09, 21.57, 20.87. HRMS (ESI) *m/z* calcd for $[M+H]^+$ $C_{18}H_{22}NO_4S$ 348.1270; found 348.1261.

4.1.5. General method for the synthesis of substituted 2-(2-(6-halo or 2,6-dihalo-9H-purin-9-yl)ethyl)-4-tosyl-3,4-dihydro-2H-benzo[b][1,4]oxazine derivatives

The corresponding tosylated derivative **15**–**17** (0.31 mmol), triphenylphosphine (164 mg, 0.63 mmol) and the appropriate 6-chloro, 2,6-dichloro or 6-bromopurine (0.34 mmol) are added to a schlenk under argon atmosphere. Then, anhydrous THF (3 mL) is added, and the reaction mixture is cooled down to −20 °C. Subsequently, DIAD (124 μL, 0.63 mmol) was added dropwise and the reaction was brought up to room temperature and stirred for 2 days. The solvent was evaporated under reduced pressure. The residue was purified by flash chromatography using EtOAc/hexane mixture in different ratios as solvent.

7-Chloro-2-(2-(6-chloro-9*H*-purin-9-yl)ethyl)-4-tosyl-3,4-dihydro-2*H*-benzo[b][1,4]oxazine (**2a**). Purification in EtOAc/hexane 1:1. White solid; 82 % yield; mp: 117°–119 °C.

^{1}H NMR (300 MHz, $CDCl_3$): δ 8.78 (s, 1H), 7.98 (s, 1H), 7.76 (d, 1H, $J = 8.9$ Hz), 7.37 (d, 2H, $J = 8.1$ Hz), 7.09 (d, 2H, $J = 8.0$ Hz), 6.96 (dd, 1H, $J_1 = 8.9$, $J_2 = 2.4$ Hz), 6.85 (d, 1H, *J*=2.4 Hz), 4.50–4.43 (m, 2H), 4.22 (dd, 1H, $J_1 = 14.9$, $J_2 = 1.8$ Hz), 3.29–3.19 (m, 2H), 2.43 (s, 3H), 2.39–2.28 (m, 1H), 2.09–2.04 (m, 1H). ^{13}C NMR (101 MHz, $CDCl_3$): δ 152.01, 151.69, 151.15, 146.52, 145.09, 144.96, 134.93, 131.62, 131.34, 129.84, 126.85, 125.31, 122.23, 121.65, 117.38, 68.53, 47.96, 40.19, 31.68, 21.62. HRMS (ESI) *m/z* calcd for $C_{22}H_{20}N_5O_3SCl_2$ $[M+H]^+$ 504.0664; found 504.0634.

7-Chloro-2-(2-(2,6-dichloro-9*H*-purin-9-yl)ethyl)-4-tosyl-3,4-dihydro-2*H*-benzo[b][1,4]oxazine (**2b**). Purification in EtOAc/hexane 1:1. White solid; 83 % yield; mp: 94°–96 °C.

^{1}H NMR (500 MHz, $CDCl_3$): δ 7.93 (s, 1H), 7.72 (d, 1H, $J = 8.9$ Hz), 7.39–7.37 (m, 2H), 7.13–7.11 (m, 2H), 6.93 (dd, 1H, $J_1 = 8.9$, $J_2 = 2.4$ Hz), 6.81 (d, 1H, H-8, $J = 2.4$ Hz), 4.42–4.39 (m, 2H), 4.18 (dd, 1H, $J_1 = 14.3$, $J_2 = 2.3$ Hz), 3.30–3.28 (m, 1H), 3.27—3.15 (m, 1H), 2.41 (s, 3H), 2.27–2.20 (m, 1H), 2.04–1.98 (m, 1H). ^{13}C NMR (126 MHz, $CDCl_3$):

δ 153.12, 153.03, 151.89, 146.43, 145.75, 145.02, 134.98, 131.37, 130.73, 129.94, 126.95, 125.28, 122.27, 121.76, 117.41, 68.65, 47.94, 40.33, 31.69, 21.62. HRMS (ESI) *m/z* calcd for $C_{22}H_{19}N_5O_3SCl_3$ $[M+H]^+$ 538.0274; found 538.0283.

7-Chloro-2-(2-(6-bromo-9*H*-purin-9-yl)ethyl)-4-tosyl-3,4-dihydro-2*H*-benzo[b][1,4]oxazine (**2c**). Purification in EtOAc/hexane 2:1. White solid; 85 % yield; mp: 172°–174 °C.

^{1}H NMR (300 MHz, $CDCl_3$): δ 8.72 (s, 1H), 7.99 (s, 1H), 7.75 (d, 1H, $J = 8.9$ Hz), 7.37 (d, 2H, *J*=8.0 Hz), 7.10 (d, 2H, $J = 8.0$ Hz), 6.95 (dd, 1H, $J_1 = 8.9$, $J_2 = 2.4$ Hz), 6.84 (d, 1H, *J*=2.4 Hz), 4.49–4.44 (m, 2H), 4.21 (dd, 1H, $J_1 = 14.0$, $J_2 = 2.0$ Hz), 3.31–3.36 (m, 2H), 2.43 (s, 3H), 2.38–2.27 (m, 1H), 2.09–2.04 (m, 1H). ^{13}C NMR (101 MHz, $CDCl_3$): δ 151.92, 150.46, 146.52, 144.96, 151.70, 134.91, 134.21, 131.31, 129.86, 126.85, 125.25, 122.22, 121.63, 117.38, 68.59, 47.95, 40.24, 31.70, 21.69. HRMS (ESI) *m/z* calcd for $C_{22}H_{20}N_5O_3SClBr$ $[M+H]^+$ 548.0159; found 548.0129.

6-Bromo-2-(2-(6-chloro-9*H*-purin-9-yl)ethyl)-4-tosyl-3,4-dihydro-2*H*-benzo[b][1,4]oxazine (**3a**). Purification in EtOAc/hexane 1:1. White solid; 83 % yield; mp: 123°–125 °C.

^{1}H NMR (400 MHz, $CDCl_3$): δ 8.78 (s, 1H), 7.99–7.98 (m, 2H), 7.43 (d, 2H, $J = 8.1$ Hz), 7.21–7.12 (m, 3H) 6.69 (d, 1H, $J = 8.1$ Hz), 4.50–4.45 (m, 2H), 4.20 (dd, 2H, $J_1 = 14.2$, $J_2 = 2.2$ Hz), 3.35 (t, 1H, $J = 9.8$ Hz), 3.23–3.17 (m, 1H), 2.44 (s, 3H), 2.38–2.31 (m, 1H), 2.10–2.08 (m, 1H). ^{13}C NMR (126 MHz, $CDCl_3$): δ 152.10, 151.69, 151.32, 145.20, 145.03, 144.92, 134.94, 129.97, 129.91, 129.13, 127.04, 126.98, 126.61, 126.59, 124.76, 118.73, 113.36, 68.76, 47.92, 40.41, 31.74, 21.66. HRMS (ESI) *m/z* calcd for $C_{22}H_{20}N_5O_3SClBr$ $[M+H]^+$ 548.0159; found 548.0139.

6-Bromo-2-(2-(2,6-dichloro-9*H*-purin-9-yl)ethyl)-4-tosyl-3,4-dihydro-2*H*-benzo[b][1,4]oxazine (**3b**). Purification in EtOAc/hexane 1:1. White solid; 85 % yield; mp: 90°–92 °C.

^{1}H NMR (500 MHz, $CDCl_3$): δ 7.98 (d, 2H, $J = 2.1$ Hz), 7.48–7.46 (m, 2H), 7.21–7.17 (m, 3H), 6.67 (d, 1H, $J = 8.7$ Hz), 4.46–4.43 (m, 2H), 4.18 (dd, 1H, $J_1 = 14.3$, $J_2 = 2.3$ Hz), 3.39–3.34 (m, 1H), 3.19 (dd, 1H, $J_1 = 14.3$, $J_2 = 9.5$ Hz), 2.44 (s, 3H), 2.30–2.22 (m, 1H), 2.10–2.03 (m, 1H). ^{13}C NMR (126 MHz, $CDCl_3$): δ 153.14, 151.04, 151.90, 145.77, 145.07, 144.94, 134.95, 130.73, 129.98, 129.12, 127.03, 126.57, 124.77, 118.73, 113.43, 68.85, 47.88, 40.45, 31.73, 21.67. HRMS (ESI) *m/z* calcd for $C_{22}H_{19}N_5O_3SCl_2Br$ $[M+H]^+$ 581.9769; found 581.9749.

6-Bromo-2-(2-(6-bromo-9*H*-purin-9-yl)ethyl)-4-tosyl-3,4-dihydro-2*H*-benzo[b][1,4]oxazine (**3c**). Purification in EtOAc/hexane 1:1. White solid; 86 % yield; mp: 183°–185 °C.

^{1}H NMR (400 MHz, $CDCl_3$): δ 8.63 (s, 1H), 8.00 (s, 1H), 7.88 (d, 1H, $J = 2.3$ Hz), 7.36–7.33 (m, 2H), 7.09 (dd, 1H, $J_1 = 8.7$, $J_2 = 2.3$ Hz) 7.05 (d, 2H, $J = 8$ Hz), 6.58 (d, 1H, *J*=8.7 Hz), 4.41–4.37 (m, 2H), 4.11 (dd, 1H, $J_1 = 14.3$, $J_2 = 2.3$ Hz), 3.30–3.25 (m, 1H), 3.13–3.07 (m, 1H), 2.41 (s, 3H), 2.34–2.19 (m, 1H), 2.02–1.96 (m, 1H). ^{13}C NMR (101 MHz, $CDCl_3$): δ 152.05, 150.45, 145.10, 145.06, 143.16, 134.90, 133.97, 129.95, 129.11, 126.98, 126.55, 124.75, 118.77, 113.32, 68.84, 47.92, 40.50, 31.76, 21.75. **HRMS** (ESI) *m/z* calcd for $C_{22}H_{19}N_5O_3SClBr_2$ $[M+Cl]^-$ 625.9264; found 625.9282.

2-(2-(6-Chloro-9*H*-purin-9-yl)ethyl)-6-methyl-4-tosyl-3,4-dihydro-2*H*-benzo[b][1,4]oxazine (**4a**). Purification in EtOAc/hexane 1:1. White solid; 83 % yield; mp: 115°–117 °C.

^{1}H NMR (400 MHz, $CDCl_3$): δ 8.77 (s, 1H), 8.00 (s, 1H), 7.63–7.62 (m, 1H), 7.38 (d, 2H, $J = 8.1$ Hz), 7.08 (d, 2H, $J = 8.1$ Hz), 6.90 (dd, 1H, $J_1 = 8.3$, $J_2 = 2.0$ Hz), 6.69 (d, 1H, $J = 8.3$ Hz), 4.49–4.45 (m, 2H), 4.19 (dd, 1H, $J_1 = 14.1$, $J_2 = 2.1$ Hz), 3.31–3.26 (m, 1H), 3.23–3.17 (m, 1H), 2.41 (s, 3H), 2.33 (s, 1H), 2.30–2.24 (m, 1H), 2.06–1.99 (m, 1H). ^{13}C NMR (126 MHz, $CDCl_3$): δ 152.06, 151.72, 151.06, 145.35, 144.64, 143.86, 135.36, 131.43, 130.98, 129.74, 127.13, 126.94, 124.53, 123.12, 116.91, 68.18, 48.36, 40.44, 31.78, 21.86, 20.89. HRMS (ESI) *m/z* calcd for $C_{22}H_{23}N_5O_3SCl$ $[M+H]^+$ 484.1210; found 484.1205.

2-(2-(2,6-Dichloro-9*H*-purin-9-yl)ethyl)-6-methyl-4-tosyl-3,4-dihydro-2*H*-benzo[b][1,4]oxazine (**4b**). Purification in EtOAc/hexane 1:1. White solid; 84 % yield; mp: 87°–89 °C.

^{1}H NMR (400 MHz, $CDCl_3$): δ 7.98 (s, 1H), 7.60 (d, 1H *J*=2.0 Hz), 7.42 (d, 2H, $J = 8.0$ Hz), 7.13 (d, 2H, $J = 8.0$ Hz), 6.89 (dd, 1H, $J_1 = 8.3$, $J_2 = 2.0$ Hz), 6.67 (d, 1H, $J = 8.3$ Hz), 4.45–4.42 (m, 2H), 4.17 (dd, 1H, $J_1 = 14.1$, $J_2 = 9.6$ Hz), 3.35–3.29 (m, 1H), 3.23–3.17 (m, 1H), 2.42 (s, 3H), 2.32 (s, 1H), 2.24–2.18 (m, 1H), 2.05–1.99 (m, 1H). ^{13}C NMR (126 MHz, $CDCl_3$): δ 153.07, 153.02, 151.73, 146.04, 144.675, 143.75, 135.37, 131.02, 130.69, 129.81, 127.79, 127.12, 126.97, 124.43, 116.90, 68.33, 48.31, 40.51, 31.75, 21.66, 20.89. HRMS (ESI) *m/z* calcd for $C_{23}H_{21}N_5O_3SCl_3$ $[M+Cl]^-$ 552.0431; found 552.0454.

2-(2-(6-Bromo-9*H*-purin-9-yl)ethyl)-6-methyl-4-tosyl-3,4-dihydro-2*H*-benzo[b][1,4]oxazine (**4c**). Purification in EtOAc/hexane 1:1. White solid; 87 % yield; mp: 160°- 162 °C.

^{1}H NMR (400 MHz, $CDCl_3$): δ 8.69 (s, 1H), 7.98 (s, 1H), 7.59 (d, 1H, *J*=2.0 Hz), 7.36 (d, 2H, *J*=8.2 Hz), 7.06 (d, 2H, *J*=8.2 Hz), 6.87 (dd, 1H, $J_1 = 8.3$, $J_2 = 2.0$ Hz), 6.66 (d, 1H, *J*=8.3 Hz), 4.45–4.41 (m, 2H), 4.18–4.13 (m, 1H), 3.29–3.25 (m, 1H), 3.27 (dd, H, $J_1 = 14.1$, $J_2 = 9.7$ Hz), 2.39 (s, 3H), 2.29 (s, 1H), 2.27–2.23 (m, 1H), 2.02–1.98 (m, 1H). ^{13}C NMR (126 MHz, $CDCl_3$): δ 151.96, 150.91, 145.27, 144.64, 143.86, 143.12, 135.35, 134.11, 130.95, 129.76, 127.12, 126.94, 124.48, 123.11, 116.93, 68.24, 48.37, 40.49, 31.81, 21.74, 20.89. HRMS (ESI) *m/z* calcd for $C_{23}H_{23}N_5O_3SBr$ $[M+H]^+$ 528.0705; found 528.0734.

4.1.6. General method for the synthesis of substituted 4-tosyl-2-((6-(trifluoromethyl)-9H-purin-9-yl)ethyl)-3,4-dihydro-2H-benzo[b][1,4]oxazine derivatives

To a solution of MFSDA (45 μL, 0.35 mmol), CuI (45.7 mg, 0.24 mmol) and HMPA (44 μL, 0.25 mmol) in anhydrous DMF (3 mL) is added the corresponding 6-bromo derivative **2c, 3c** or **4c** (0.2 mmol). This mixture is placed in the microwave at 150° for 15 min. Then, Ethyl acetate is added and the solution is washed with saturated solutions of NH_4Cl, $NaHCO_3$, H_2O and brine. The organic layer is dried over anhydrous Na_2SO_4, filtered and evaporated under vacuum. After that, the reaction crude is purified by flash chromatography (EtOAc/hexane 1:1).

7-Chloro-2-(2-(6-(trifluoromethyl)-9*H*-purin-9-yl)ethyl)-4-tosyl-3,4-dihydro-2*H*-benzo[b][1,4]oxazine (**2d**). White solid; 80 % yield; mp: 120°–122 °C.

^{1}H NMR (400 MHz, $CDCl_3$): δ 9.11 (s, 1H), 8.13 (s, 1H), 7.75 (dd, 1H, $J_1 = 8.8$ Hz, $J_2 = 1.6$ Hz), 7.40 (d, 2H, *J*=7.9 Hz), 7.13 (d, 2H, $J = 7.9$ Hz), 6.95 (dd, 1H, $J_1 = 8.9$, $J_2 = 2.1$ Hz), 6.82 (d, 1H, *J*=1.6 Hz), 4.59–4.50 (m, 2H), 4.22 (dd, 1H, $J_1 = 14.4$, $J_2 = 2.3$ Hz), 3.40 (t, 1H, $J = 9.8$), 3.22 (dd, 1H, $J_1 = 14.4$, $J_2 = 9.8$ Hz), 2.41 (s, 3H), 2.33–2.28 (m, 1H), 2.12–2.06 (m, 1H). ^{13}C NMR (101 MHz, $CDCl_3$): δ 153.75, 152.05, 147.22, 146.47, 145.02, 135.05, 131.38, 130.05, 129.94, 126.95, 125.21, 122.27, 121.74, 119.01, 117.41, 68.86, 47.98, 40.15, 31.86, 21.52. HRMS (ESI) *m/z* calcd for $C_{23}H_{20}N_5O_3SClF_3$ $[M+H]^+$ 538.0927; found 538.0931.

6-Bromo-2-(2-(6-(trifluoromethyl)-9H-purin-9-yl)ethyl)-4-tosyl-3,4-dihydro-2H-benzo[b][1,4]oxazine (**3d**). White solid; 78 % yield; mp: 188°–190 °C.

^{1}H NMR (400 MHz, $CDCl_3$): δ 9.10 (s, 1H), 8.15 (s, 1H), 7.96 (d, 1H, $J = 2.3$ Hz), 7.46 (d, 2H, $J = 8.0$ Hz), 7.19–7.16 (m, 2H), 6.65 (d, 1H, *J*=8.7 Hz), 4.58–4.49 (m, 2H), 4.21 (dd, 1H, $J_1 = 14.3$, $J_2 = 2.4$ Hz), 3.52–3.43 (m, 1H), 3.22 (dd, 1H, $J_1 = 14.3$, $J_2 = 9.5$ Hz), 2.42 (s, 3H), 2.35–2.27 (m, 1H), 2.16–2.06 (m, 1H). ^{13}C NMR (101 MHz, $CDCl_3$): δ 153.76, 152.03, 147.28, 145.06, 144.97, 135.02, 132.31, 129.98, 129.09, 127.03, 126.45, 124.79, 119.18, 118.71, 113.39, 69.09, 47.91, 40.26, 31.86, 21.53. HRMS (ESI) *m/z* calcd for $C_{23}H_{19}N_5O_3SCl\ BrF_3$ $[M+Cl]^-$ 616.0033; found 616.0056.

6-Methyl-4-tosyl-2-(2-(6-(trifluoromethyl)-9H-purin-9-yl)ethyl)-3,4-dihydro-2H-benzo[b][1,4]oxazine (**4d**). White solid; 80 % yield; mp: 177°–179 °C.

^{1}H NMR (500 MHz, $CDCl_3$): δ 8.42 (s, 1H), 7.63–7.62 (m, 2H), 7.46 (d, 2H, $J = 7.4$ Hz), 7.14 (d, 2H, $J = 7.4$ Hz), 6.89 (dd, 1H, $J_1 = 8.3$, $J_2 = 2.0$ Hz), 6.73 (d, 1H, $J = 8.3$ Hz), 4.41–4.28 (m, 2H), 4.19 (dd, 1H, $J_1 = 14.2$, $J_2 = 2.4$ Hz), 3.42–3.36 (m, 1H), 3.21–3.16 (m, 1H), 2.39 (s, 3H), 2.33 (s, 1H), 2.27–2.19 (m, 1H), 2,03–1.94 (m, 1H). ^{13}C NMR (126

MHz, $CDCl_3$): δ 153.70, 151.20, 147.54, 144.30, 144.27, 138.85, 135.47, 132.14,130.76, 129.80, 127.04, 126.91, 124.29, 123.25, 120.00, 116.99, 68.51, 48.49, 39.81, 32.15, 21.51, 20.89. HRMS (ESI) *m/z* calcd for $C_{24}H_{22}N_5O_3F_3NaS$ $[M+Na]^+$ 540.1293; found 540.1324.

4.2. Biology

4.2.1. Cell culture

HCT-116 colorectal carcinoma and MCF-7 breast cancer cell lines were provided by the Cell Bank of the University of Granada. Cells were grown in Dulbecco's modified Eagle's medium (DMEM) (Sigma, St. Louis, MO, USA), supplemented with 10 % fetal bovine serum (FBS) and 1 % penicillin/streptomycin (P/S) (Sigma, St. Louis, MO, USA), under air containing 5 % CO2 in an incubator at 37 °C. All the cell lines were passaged for less than 6 months and routinely assayed for mycoplasma contamination.

4.2.2. Drug treatment

Compounds **3a–l** were dissolved in DMSO and stored at −20 °C. For each experiment, the stock solutions were further diluted in medium to obtain the desired concentrations. The final solvent concentration in cell culture was ≤0.1 % v/v of DMSO, a concentration without any effect on cell replication. Parallel cultures of MCF-7 and HCT-116 cells in medium with DMSO were used as controls.

4.2.3. In vitro cytotoxicity assays

The effect of the compounds 3a-l on cell viability was assessed using the Thiazolyl Blue Tetrazolium Bromide (TBTB) (Sigma, St. Louis, MO, USA) colorimetric assay (MTT). Cells (2500 cells/well) were seeded on 96-well plates, incubated for 24 h and then treated with different drug concentrations. Three days later, the wells were treated by TBTB for 3 h, followed by dimethyl sulfoxide (DMSO) dissolution (≥99.5 %) (Sigma-Aldrich, Saint-Quentin Fallavier, France). Cells were processed using a Titertek Multiscan apparatus (Flow, Irvine, CA, USA) at 570 nm. IC_{50} values were estimated using the 4-parameter logistic function included in the "drc"[50] package from R[51] statistical software.

4.2.4. Kinase inhibition assays

The kinase inhibition profile of compounds **2b**, **2c**, **3b, 4b** and **4c** was defined using a panel of 9 protein kinases (Table S1 Supplementary data). Residual activity values were measured by testing each compound at two concentrations (5×10^{-5} and 5×10^{-6} M) in singlicate for each kinase assay. Detailed methods por kinome analyses are given in Suplementary data.

4.2.5. Microscopy analysis.

HCT-116 and MCF-7 cell line were seeded in 24-well plates on tissue culture coverslips (13 mm) and incubated for 24 h. The cells were then treated for 12 h with the **2b** and **4b** compounds at a concentration of 50 μM. The cells were washed in ice-cold PBS, fixed and prepared for scanning electron microscopy (SEM) according to standard protocol (Hitachi S-800, Hitachi, Tokyo, Japan) as described in.[52]

4.2.6. Annexin V apoptosis assay

Cells were seeded in 6-well plates for 24 h and then treated for 12 h with the **2b** and **4b** compounds at a concentration of 50 μM. Cells were trypsinized and analyzed using an annexin V-fluorescein isothiocyanate detection kit (eBioscience Inc., San Diego, CA, USA) according to the manufacturer's instructions. The samples were immediately processed using a FACSAria III flow cytometer (Becton Dickinson, BD Biosciences) from the Scientific Instrumental Center (University of Granada).

4.2.7. Cell cycle analysis

Cell cycle phases (G0/G1, S, or G2/M) were characterized according to cellular DNA content. Fluorescence dye propidium iodide (PI) (Sigma) binds with DNA strongly at a ratio of 1:1; hence, DNA contents of the cell cycle phases had varied PI fluorescent intensities (PI) excited by a 488 nm solid-state laser, the fluorescent emission being captured in a detector with a band pass (BP) 585 ± 20 nm filter). Cell cultures previously seeded and treated during 12 h with 50 μM of **2b** and **4b** compounds were harvested, washed twice with phosphate-buffered saline (PBS), and fixed in 70 % ice-cold ethanol at 4 °C during 30 min. Cell pellets were washed twice with PBS and resuspended in a PI/RNase Staining Buffer (BD Pharmingen, San Diego, CA, USA) according to manufacturer's instructions. The percentage of cells in G0/G1, S, and G2/M phases was determined by FACS (fluorescence-activated cell sorting) using a FACSCalibur flow cytometer (BD Biosciences, Franklin Lakes, NJ, USA).

4.2.8. Statistical analysis

Data presented in this work were performed in triplicate and compared with Student's t-tests. All data are expressed as the mean ± SD. p-values < 0.05 (*), p-values < 0.01 (**), and p-values < 0.001 (***).

4.3. Docking studies

Docking analysis was carried out using Autodock 4.2.6 (AD4)[53] on the human epidermal growth factor receptor 2 (hHER2, pdb ID 3RCD, subunit B) and the human mitogen-activated protein kinase 8 (hJNK1, pdb ID 4AWI). Both enantiomers of the ligands structures were built on Avogadro[54] and optimized using Gaussian software (HF/6-31G(d,p)).[55] Once optimized, ligands PDB files were prepared for docking using the prepare_ligand4.py script included MGLTools 1.5.4.[53] Protein structure, were prepared for docking using the PDB2PQR tools[56] Water and ligand molecules were removed and charges and non-polar hydrogen atoms were added at pH 7.0. The produced structures were saved as a pdb files and prepared for docking with AD4 using the prepare_receptor4.py script from MGLTools. The docking grid was centered on the orthosteric site of hHER2 and hJNK1 and set with the following grid parameters: 75 Å × 80 Å × 70 Å with 0.375 Å spacing. In all calculations, AD4 parameter file was set to 100 GA runs, 2.500.000 energy evaluations and a population size of 150. The Lamarckian genetic algorithm local search (GALS) method was used for the docking calculations. All dockings were performed with a population size of 250 and a Solis and Wets local search of 300 rounds was applied with a probability of 0.06. A mutation rate of 0.02 and a crossover rate of 0.8 were used. The docking results from each of the 100 calculations were clustered based on root-mean square deviation (RMSD) solutions differing by less than 2.0 Å between the Cartesian coordinates of the atoms and ranked based on free energy of binding. The obtained conformations were individually inspected and figures were created with UCSF Chimera 1.15.[57]

CRediT authorship contribution statement

Ana Conejo-García: Writing – review & editing, Writing – original draft, Visualization, Validation, Supervision, Project administration, Methodology, Funding acquisition, Formal analysis, Data curation, Conceptualization. **Yaiza Jiménez-Martínez:** Validation, Methodology, Investigation, Data curation. **Rubén Cámara:** Methodology, Investigation. **Francisco Franco-Montalbán:** Writing – review & editing, Writing – original draft, Software, Methodology. **Jesús Peña-Martín:** Methodology, Investigation. **Houria Boulaiz:** Writing – review & editing, Writing – original draft, Supervision, Methodology, Formal analysis. **M. Dora Carrión:** Writing – review & editing, Writing – original draft, Visualization, Validation, Supervision, Project administration, Methodology, Investigation, Formal analysis, Data curation, Conceptualization.

Declaration of competing interest

The authors declare that they have no known competing financial interests or personal relationships that could have appeared to influence

the work reported in this paper.

Data availability

Data will be made available on request.

Acknowledgements

The authors thank the Centro de Supercomputación de la Universidad de Granada (CSIRC) for the computing resources.

This work was funded by the project PID2021.128109OB.I00 financed by MICIU/AEI/doi: 10.13039/501100011033 and for FEDER, UE.

The authors thank the Granada University Library for the financial support to the APC.

Appendix A. Supplementary data

Supplementary data to this article can be found online at https://doi.org/10.1016/j.bmc.2024.117849.

References

1. Bray F, Laversanne M, Sung H, et al. Global cancer statistics 2022: GLOBOCAN estimates of incidence and mortality worldwide for 36 cancers in 185 countries. *CA: A Cancer J Clin*. 2024;74:229–263. https://doi.org/10.3322/caac.21834.
2. Victoir B, Croix C, Gouilleux F, et al. Targeted therapeutic strategies for the treatment of cancer. *Cancers*. 2024;16:461. https://doi.org/10.3390/cancers16020461.
3. Biller LH, Schrag D. Diagnosis and treatment of metastatic colorectal cancer: a review. *J Am Med Assoc*. 2021;325:669–685. https://doi.org/10.1001/jama.2021.0106.
4. Powers-James C, Morse M, Narayanan S, et al. Integrative oncology approaches to reduce recurrence of disease and improve survival. *Curr Oncol Rep*. 2024;26:147–163. https://doi.org/10.1007/s11912-023-01467-5.
5. Dell' Aversana C, Sarno F, Benedetti R, et al. Cancer therapy resistance: choosing kinase inhibitors. *Pharmaceutics*. 2024;16:373. https://doi.org/10.3390/pharmaceutics16030373.
6. Khelwatty SA, Puvanenthiran S, Essapen S, et al. HER2 expression is predictive of survival in cetuximab treated patients with RAS wild type metastatic colorectal cancer. *Cancers*. 2021;13:638. https://doi.org/10.3390/cancers13040638.
7. Iqbal N, Iqbal N. Human epidermal growth factor receptor 2 (HER2) in cancers: overexpression and therapeutic implications. *Mol Biol Int*. 2014;2014:1–9. https://doi.org/10.1155/2014/852748.
8. Cruz-López O, Ner M, Nerín-Fonz F, et al. Design, synthesis, HER2 inhibition and anticancer evaluation of new substituted 1,5-dihydro-4,1-benzoxazepines. *J Enzyme Inhib Med Chem*. 2021;36:1551–1561. https://doi.org/10.1080/14756366.2021.1948841.
9. Li W, Wen C, Bai H, et al. JNK signaling pathway is involved in piperlongumine-mediated apoptosis in human colorectal cancer HCT116 cells. *Oncol Lett*. 2015;10:709–715. https://doi.org/10.3892/ol.2015.3371.
10. Miller SM, Goulet DR, Johnson GL. Targeting the breast cancer kinome. *J Cell Physiol*. 2017;232:53–60. https://doi.org/10.1002/jcp.25427.
11. De Schutter E, Cappe B, Wiernicki B, et al. Plasma membrane permeabilization following cell death: many ways to dye!. *Cell Death Discov*. 2021;7:183. https://doi.org/10.1038/s41420-021-00545-6.
12. Zhang Y, Chen X, Gueydan C, et al. Plasma membrane changes during programmed cell deaths. *Cell Res*. 2018;28:9–21. https://doi.org/10.1038/cr.2017.133.
13. Galluzzi L, Vitale I, Aaronson SA, et al. Molecular mechanisms of cell death: recommendations of the nomenclature committee on cell death. *Cell Death Differ*. 2018;25:486–541. https://doi.org/10.1038/s41418-017-0012-4.
14. Vandenabeele P, Bultynck G, Savvides SN. Pore-forming proteins as drivers of membrane permeabilization in cell death pathways. *Nat Rev Mol Cell Biol*. 2023;24:312–333. https://doi.org/10.1038/s41580-022-00564-w.
15. Mishchenko T, Balalaeva I, Gorokhova A, et al. Which cell death modality wins the contest for photodynamic therapy of cancer? *Cell Death Dis*. 2022;13:455. https://doi.org/10.1038/s41419-022-04851-4.
16. Song T, Lee M, Bae I, et al. Synthesis and evaluation of a 3,4-dihydro-2H-benzoxazine derivative as a potent CDK9 inhibitor for anticancer therapy. *Bull Kor Chem Soc*. 2021;42:416–419. https://doi.org/10.1002/bkcs.12204.
17. Bollu R, Palem JD, Bantu R, et al. Rational design, synthesis and anti-proliferative evaluation of novel 1,4-benzoxazine-[1,2,3]triazole hybrids. *Eur J Med Chem*. 2015;89:138–146. https://doi.org/10.1016/j.ejmech.2014.10.051.
18. Gambacorta N, Gasperi V, Guzzo T, et al. Exploring the 1,3-benzoxazine chemotype for cannabinoid receptor 2 as a promising anti-cancer therapeutic. *Eur J Med Chem*. 2023;259, 115647. https://doi.org/10.1016/j.ejmech.2023.115647.
19. Jana AK, Singh J, Ganesher A, et al. Tyrosine-derived novel benzoxazine active in a rat syngenic mammary tumor model of breast cancer. *J Med Chem*. 2021;64:16293–16316. https://doi.org/10.1021/acs.jmedchem.1c01624.
20. Hoelscher P, Jautelat R, Rehwinkel H, et al. Benzoxazine derivatives and Benzothiazine derivatives having NOS-inhibitory and Antioxidant properties. WO0181324A1; November 1, 2001. <https://worldwide.espacenet.com/patent/search/family/007640466/publication/WO0181324A1?q=pn%3DWO0181324>.
21. Hoelscher P, Rehwinkel H, Jaroch S, et al. Benzoxazine and Benzothiazine derivatives and their use in medicine. WO0017173 A1; March 30, 2000. <https://worldwide.espacenet.com/patent/search/family/007882416/publication/WO0017173A1?q=pn%3DWO0017173A1>.
22. Fernández-Sáez N, Rubio-Ruiz B, Campos JM, Unciti-Broceta A, Carrión MD, Camacho ME. Purine derivatives with heterocyclic moieties and related analogs as new antitumor agents. *Future Med Chem*. 2019;11:83–95. https://doi.org/10.4155/fmc-2018-0291.
23. Punirun T, Soorukram D, Kuhakarn C, et al. Stereoselective synthesis of 1-fluoro-exo, exo-2,6-diaryl-3,7-dioxabicyclo[3.3.0]octanes: synthesis of (±)-1-Fluoromembrine. *J Org Chem*. 2015;80:7946–7960. https://doi.org/10.1021/acs.joc.5b00970.
24. Hameed A, Javed S, Noreen R, et al. Facile and green synthesis of saturated cyclic amines. *Molecules*. 2017;22. https://doi.org/10.3390/molecules22101691.
25. Kumara Swamy KC, Bhuvan Kumar NN, Balaraman E, et al. Mitsunobu and related reactions: advances and applications. *Chem Rev*. 2009;109:2551–2651. https://doi.org/10.1021/cr800278z.
26. Clarke SL, McGlacken GP. Methyl fluorosulfonyldifluoroacetate (MFSDA): an underutilised reagent for trifluoromethylation. *Chem Eur J*. 2017;23:1219–1230. https://doi.org/10.1002/chem.201602511.
27. Puhalla S, Brufsky A. Treatment of HER2-positive breast cancer: looking backwards briefly. *Lancet Oncol*. 2013;14:1250–1251. https://doi.org/10.1016/s1470-2045(13)70536-9.
28. Yao GD, Ge MY, Li DQ, et al. L-A03, a dihydroartemisinin derivative, promotes apoptotic cell death of human breast cancer MCF-7 cells by targeting c-Jun N-terminal kinase. *Biomed Pharmacother*. 2018;105:320–325. https://doi.org/10.1016/j.biopha.2018.05.093.
29. Song C, Xu W, Wu H, et al. Photodynamic therapy induces autophagy-mediated cell death in human colorectal cancer cells via activation of the ROS/JNK signaling pathway. *Cell Death Dis*. 2020;11. https://doi.org/10.1038/s41419-020-03136-y.
30. Arter C, Trask L, Ward S, Yeoh S, Bayliss R. Structural features of the protein kinase domain and targeted binding by small-molecule inhibitors. *J Biol Chem*. 2022;298:10224. https://doi.org/10.1016/j.jbc.2022.102247.
31. Ishikawa T, Seto M, Banno H, et al. Design and synthesis of novel human epidermal growth factor receptor 2 (HER2)/epidermal growth factor receptor (EGFR) dual inhibitors bearing a pyrrolo[3,2-d]pyrimidine scaffold. *J Med Chem*. 2011;54:8030–8050. https://doi.org/10.1021/jm2008634.
32. Yu P, Zhang X, Liu N, et al. Pyroptosis: mechanisms and diseases. *Signal Transduct Target Ther*. 2021;6. https://doi.org/10.1038/s41392-021-00507-5.
33. Zhang Y, Chen X, Gueydan C, et al. Plasma membrane changes during programmed cell deaths. *Cell Res*. 2018;28:9–21. https://doi.org/10.1038/cr.2017.133.
34. Chen X, He WT, Hu L, et al. Pyroptosis is driven by non-selective gasdermin-D pore and its morphology is different from MLKL channel-mediated necroptosis. *Cell Res*. 2016;26:1007–1020. https://doi.org/10.1038/cr.2016.100.
35. Kari S, Subramanian K, Altomonte IA, et al. Programmed cell death detection methods: a systematic review and a categorical comparison. *Apoptosis*. 2022;27:482–508. https://doi.org/10.1007/s10495-022-01735-y.
36. Kumaraswamy KL, Archana M, Bastian TL, et al. Various methods available for detection of apoptotic cells. A review. *Indian J Cancer*. 2013;50(3):274–283. https://doi.org/10.4103/0019-509x.118720.
37. Feng Y, Huang X. Methodology for comprehensive detection of pyroptosis. *Methods Mol Biol*. 2021;2255:149–157. https://link.springer.com/protocol/10.1007/978-1-0716-1162-3_13.
38. Yu P, Zhang X, Liu N, et al. Pyroptosis: mechanisms and diseases. Signal transduct. *Target Ther*. 2021;6:128. https://doi.org/10.1038/s41392-021-00507-5.
39. Boulaiz H, Aránega A, Cáceres B, et al. A novel double-enhanced suicide gene therapy in a colon cancer cell line mediated by gef and apoptin. *BioDrugs*. 2014;28:63–74. https://doi.org/10.1007/s40259-013-0055-0.
40. Ramírez A, Conejo-García A, Griñán-Lisón C, et al. Enhancement of tumor cell death by combining gef gene mediated therapy and new 1,4-benzoxazepin-2,6-dichloro-purine derivatives in breast cancer cells. *Front Pharmacol*. 2018;9:798. https://doi.org/10.3389/fphar.2018.00798.
41. van Niekerk A, Chakraborty S, Bellis C, et al. Binuclear palladacycles with ionisable and non-ionisable tethers as anticancer agents. *J Inorg Biochem*. 2024;257, 112608. https://doi.org/10.1016/j.jinorgbio.2024.112608.
42. Silva MT. Secondary necrosis: the natural outcome of the complete apoptotic program. *FEBS Lett*. 2010;584:4491–4499. https://doi.org/10.1016/j.febslet.2010.10.046.
43. Sachet M, Liang YY, Oehler R. The immune response to secondary necrotic cells. *Apoptosis*. 2017;22:1189–1204. https://doi.org/10.1007/s10495-017-1413-z.
44. Rogers C, Fernandes-Alnemri T, Mayes L, et al. Cleavage of DFNA5 by caspase-3 during apoptosis mediates progression to secondary necrotic/pyroptotic cell death. *Nat Commun*. 2017;8:14128. https://doi.org/10.1038/ncomms14128.
45. Galluzzi L, Kroemer G. Secondary necrosis: accidental no more. *Trends Cancer*. 2017;3:1–2. https://doi.org/10.1016/j.trecan.2016.12.001.
46. Liu Y, Niu R, Zhang X, et al. Metal-organic framework-based nanovaccine for relieving immunosuppressive tumors via hindering efferocytosis of macrophages and promoting pyroptosis and cuproptosis of cancer cells. *ACS Nano*. 2024;18:12386–12400. https://doi.org/10.1021/acsnano.4c0151.
47. Hamed OA, El-Sayed NAE, Mahmoud WR, et al. Molecular docking approach for the design and synthesis of new pyrazolopyrimidine analogs of roscovitine as potential

CDK2 inhibitors endowed with pronounced anticancer activity. *Bioorg Chem*. 2024; 147, 107413. https://doi.org/10.1016/j.bioorg.2024.107413.
48. Liu Y, Li F, Wang Q, et al. Anlotinib inhibits growth of human esophageal cancer TE-1 cells by negative regulating PI3K/Akt signaling pathway. *Discov Oncol*. 2024;15: 134. https://doi.org/10.1007/s12672-024-00995-1.
49. Moreno-Quintero G, Castrillón-Lopez W, Herrera-Ramirez A, et al. Synthesis and chemopreventive potential of 5-FU/genistein hybrids on colorectal cancer cells. *Pharmaceuticals*. 2022;15:1299. https://doi.org/10.3390/ph15101299.
50. Ritz C, Baty F, Streibig JC, et al. Dose-response analysis using R. *PLoS One*. 2015;10: e0146021. https://doi.org/10.1371/journal.pone.014602.
51. R Core Team. R: a language and environment for statistical computing. r foundation for statistical computing. R. Foundation for statistical computing, Vienna, Austria. https://www.R-project.org/.
52. Jiménez-Martínez Y, Griñán-Lisón C, Khaldy H, et al. LdrB toxin with in vitro and in vivo antitumor activity as a potential tool for cancer gene therapy. *Cancers*. 2019;11: 1016. https://doi.org/10.3390/cancers11071016.
53. Morris GM, Huey R, Lindstrom W, et al. AutoDock4 and AutoDockTools4: automated docking with selective receptor flexibility. *J Comput Chem*. 2009;30: 2785–2791. https://doi.org/10.1002/jcc.21256.
54. Hanwell MD, Curtis DE, Lonie DC, Vandermeersch T, Zurek E, et al. Avogadro: an advanced semantic chemical editor, visualization, and analysis platform. *J Cheminf*. 2012;4:17. https://doi.org/10.1186/1758-2946-4-17.
55. Frisch MJ, Trucks GW, Schlegel HB, et al. Fox, GAUSSIAN 09 (Revision D.1). GAUSSIAN 09 (Revision B.01); 2010.
56. Dolinsky TJ, Nielsen JE, McCammon JA, Baker NA. PDB2PQR: an automated pipeline for the setup of Poisson-Boltzmann electrostatics calculations. *Nucl Acids Res*. 2004;32:W665–W667. https://doi.org/10.1093/nar/gkh381.
57. Pettersen EF, Goddard TD, Huang CC, et al. UCSF chimera – a visualization system for exploratory research and analysis. *J Comput Chem*. 2004;25:1605–1612. https://doi.org/10.1002/jcc.20084.